Completely Elastic Deformation of Hydrogenated Ta Thin Films

Bannenberg, Lars J.; Blom, Larissa; Sakaki, Kouji; Asano, Kohta; Schreuders, Herman

DOI
10.1021/acsmaterialslett.3c00038

Publication date
2023

Document Version
Final published version

Published in
ACS Materials Letters

ACS MATERIALS LETTERS

www.acsmaterialsletters.org

LETTER

Completely Elastic Deformation of Hydrogenated Ta Thin Films

Lars J. Bannenberg,* Larissa Blom, Kouji Sakaki, Kohta Asano, and Herman Schreuders

Cite This: *ACS Materials Lett.* 2023, 5, 962−969

Read Online

ACCESS | Metrics & More | Article Recommendations | Supporting Information

ABSTRACT: Nanostructured metal hydrides could play a key role in a hydrogen economy. The nanostructuring or confinement of these materials as, e.g., thin films significantly affects the structural and functional properties. For tantalum hydride, a versatile hydrogen sensing material, we show that the confinement of tantalum as a thin film extends the solubility limit by suppressing the phase transition observed in bulk upon hydrogenation. Different from bulk, the body centered cubic unit cell continuously deforms with unequal lattice constants and angles between lattice vectors. This deformation ensures that the volumetric expansion is realized in the out-of-plane direction, and surprisingly, completely elastic in nature. The first-order phase transition suppression combined with the continuous elastic deformation of the tantalum unit cell over an extraordinary wide solubility range ensures the superb performance of tantalum and its alloys as a hysteresis-free optical hydrogen sensing range over a hydrogen pressure/concentration range of over 7 orders of magnitude.

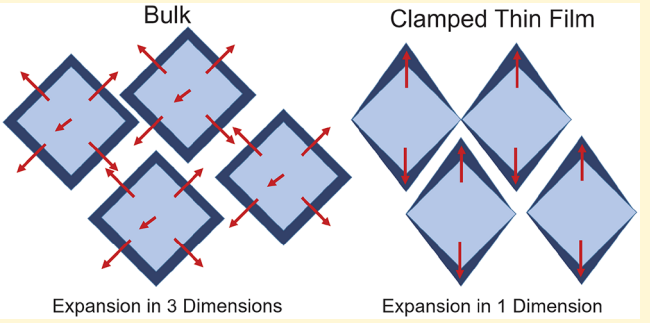

Hydrogen is projected to play a paramount role in the future green society as both an energy vector and a feedstock for the chemical industry. In such a hydrogen powered economy, metal hydrides may play an important role. Although long considered as a potential hydrogen storage medium,[1−3] metal hydrides are now researched for use in fuel cells,[4] hydrogen purifying membranes,[5,6] solid-state electrolytes,[3,7] batteries,[8] switchable mirrors,[9,10] and especially hydrogen sensors.[3,11−16]

Often, the application of metal hydrides relies on nanostructured materials which may have significantly different structural and functional properties than their bulk counterparts. Nanostructuring and nanoconfinement may change the stability and the occurrence of phases and phase transitions (see, e.g., refs 17−25). These effects can typically be the result of increased surface-to-volume ratios altering the thermodynamics of the system or geometric constraints on possibilities to expand volumetrically such as clamping to the supporting substrate. The latter effect is particularly relevant for thin films. In the case of materials for hydrogen sensors, metal hydrides are typically structured as thin films or nanoparticles.[3,13−16] For this application in particular, the understanding of the occurrence and nature of phase transitions is crucial for realizing hysteresis-free hydrogen sensing materials that are stable over time and repeated exposure to hydrogen.

Tantalum and especially its alloys have recently been identified as an exceptionally versatile hydrogen sensing material.[26−28] At room temperature, the material provides a hysteresis-free and exceptionally reproducible change in optical transmission when exposed to hydrogen over at least 7 orders of magnitude in hydrogen concentration. This is surprising, as below its critical temperature of $T_C \approx 61$ °C, a sequence of phase transitions may occur when bulk tantalum is exposed to hydrogen.[29,30] Tantalum itself crystallizes in a body-centered-cubic (bcc) structure and forms for $T > T_C$ a solid solution with hydrogen where hydrogen occupies the tetrahedral sites. At temperatures around room temperature, at least two orthorhombic phases exist: an orthorhombic phase were the hydrogen atoms are partially ordered and one orthorhombic phase, close to stochiometric $TaH_{0.5}$, in which the hydrogen atoms are fully ordered. All these phases are separated by two-phase regions, indicating first-order transitions with associated hysteresis, as confirmed by heat capacity and electrical resistivity measurements.[29,31,32] These first-order phase transitions are at variance with the observed hysteresis-free sensing range of thin film tantalum at room temperature. As such, it could imply either that the critical temperature is reduced in

Received: January 10, 2023
Accepted: February 24, 2023

thin film tantalum and a solid solution of hydrogen and tantalum is formed at room temperature or that the nature of the transition changed from first to second order, thereby eliminating the hysteresis. The study of phase transitions in thin films, and answering this question in particular, are usually complicated by the strong texture of the films. Whereas X-ray diffraction (XRD) on powders supplies information on several lattice reflections, Bragg−Brentano XRD measurements of thin films supply information solely on the out-of-plane direction: in the case of tantalum-hydride, only the {110} (and higher order multiples) can be observed, preventing precise phase identification.

To elucidate the structure of tantalum−hydrogen thin films, we employ in situ out-of-plane, in-plane XRD, and X-ray and neutron reflectometry (XRR/NR). We show that even at room temperature a solid solution of tantalum and hydrogen exists up to at least $TaH_{0.8}$. Upon hydrogenation, the tantalum unit cell is continuously deformed, expanding predominantly in the out-of-plane direction. Surprisingly, this deformation is completely elastic over the entire hydrogen solubility range. The suppression of the first-order phase transitions and the purely elastic deformation upon hydrogenation are important results, as they enable the excellent performance of tantalum as a hysteresis-free hydrogen sensing material. Taking a wider view, our results underscore the significant effect of nano-confinement on the structural and functional properties of thin films and other nanostructured metal hydrides.

EXPERIMENTAL SECTION

The Ta thin film samples studied here consist of a 4 nm titanium adhesion layer, a 40 nm Ta sensing layer, and a 10 nm $Pd_{0.6}Au_{0.4}$ capping layer. The purpose of the capping layer is 2-fold: it promotes the hydrogen dissociation reaction and protects the tantalum layer from, e.g., oxidation or nitridation. The three layers are produced by magnetron sputtering inside a vacuum chamber (AJA Int., Scituate, MA, USA) in 0.3 Pa of Ar. The base pressure of the vacuum chamber is 10^{-6} Pa. During the deposition, the substrates were continuously rotated to enhance the homogeneity. Two different substrates have been used: for the X-ray measurements, we used 0.5 mm thick 10 × 10 mm^2 fused quartz substrates and roughness <0.4 nm (Mateck GmbH, Jülich, Germany). For the neutron reflectometry measurements, 3.0 mm thick fused quartz substrates were used with a diameter of 76.2 mm (Coresix Precision Glass, Inc., VA, United States of America). These tailor-made substrates have a flatness of 2 lambda over 85% CA Central and a surface roughness <0.5 nm.

To deposit the layers, we used targets with a purity of >99.9% and a diameter of 50.8 mm (2 in.) (Mateck GmbH, Jülich, Germany). To prevent oxidation and nitridation of the Ta target, we stored this target in an Ar-filled glovebox. As an additional precaution, we presputtered this target for 60 min before use. The deposition rates and powers were 0.05 and 0.10 nm s^{-1} and 100 and 125 DC for Ti and Ta, respectively. The $Pd_{0.6}Au_{0.4}$ capping layer was produced using codepositing Pd (50 W DC) and Au (25 W DC) with a rate of 0.13 nm s^{-1}. All rates are determined by sputtering each element separately for a well-defined time interval on a substrate. Then, these tooling samples were analyzed using X-ray reflectometry (XRR) to obtain the thickness of the deposited layer. Using the thickness and the deposition time, we then calculated the sputter rate.

Before all measurements, we (un)loaded the films three times by subsequently exposing the samples to $P_{H_2} = 10^{+6}$ Pa at T = 28 °C inside the hydrogenography setup (see, e.g., ref 28 for more details). Optical transmission measurements show that reproducible results that are completely free of hysteresis are found after the first cycle. Differences between the first and following cycles are relatively common for thin film metal hydrides and arise from the settling of the microstructure. The morphology of the sample was characterized after exposure to hydrogen using a Bruker multimode atomic force microscope (AFM) (Figure S1). The measurements indicate no mesopores or holes in the film and show a smooth surface with a root-mean-square (rms) roughness of approximately 1 nm. This roughness agrees well with XRR measurements that indicate a roughness of 1 nm. Both measurements also indicate that no delamination of the film from the substrate occurred. In particular, this would have resulted in an XRR measurement without any fringes.

All X-ray diffraction (XRD) and X-ray reflectometry (XRR) measurements were carried out using a Bruker D8 Discover (Cu Kα, λ = 0.1542 nm) featuring a LYNXEYE XE detector (Bruker AXS, Karlsruhe, Germany) operating in 0D mode. For the out-of-plane XRD measurements, a configuration was used with a Göbel mirror to generate a parallel X-ray beam and a 0.1 mm fixed exit slit to control the footprint/resolution on the primary side. On the secondary side, two 0.1 mm slits were used to control the resolution.

The in situ XRD and XRR measurements were carried out by placing the sample inside an Anton Paar XRK900 Reactor chamber with a base pressure of $P < 5 \times 10^{-4}$ mbar. Temperature control was achieved with an Anton Paar TCU 700 control unit (Anton Paar GmbH, Graz, Austria). To control the partial hydrogen pressure, we vary the absolute pressure of 0.1% or 4.0% H_2 in He gas between 11 mbar and 6.1 bar ($\Delta c_{H_2}/c_{H_2} < 2\%$, Linde Gas Benelux BV, Dieren, The Netherlands) using a pressure control unit (MKS instrument including a type 250 controller, Andover, MA, United Stated of America). This pressure control unit is connected to a manometer (MKS instrument including a Baratron type 627DMCC1B) mounted to the inlet of the reactor chamber and which controls the pressure using a solenoid inlet valve (MKS instrument 0248AC-10000SV) and a manometer (MKS instrument including a Baratron type 627DMCC1B). To ensure a constant flow of at least 10 sccm during the measurements, a mass flow controller (Brooks Instruments 150 sccm, Hatfield, PA, United States of America) is connected to the outlet of the reactor chamber and a vacuum pump (Adixen Drytel 1025, Pfeiffer Vacuum GmbH, Asslar, Germany). A solenoid outlet valve (MKS instrument including 0248AC-10000SV, Andover, MA, connected to a Delta Elektronica ES030-5 Power Supply, Zierikzee, The Netherlands) is positioned parallel to the flow controller to guarantee enough flow at relatively low (P < 1 kPa) absolute pressures. A home-written National Instruments Labview code is used to automatically control the pressure control unit, flow controller, and outlet valve.

The in situ in-plane XRD measurements were performed at a tilting angle χ = 30, 45, and 60°, where the tilt was in the plane perpendicular to the X-ray beam. To enable this, sample holders were 3D printed that allowed the samples to be oriented under different tilting angles χ inside the reactor chamber. As these sample holders increase the height of the

https://doi.org/10.1021/acsmaterialslett.3c00038
ACS Materials Lett. 2023, 5, 962−969

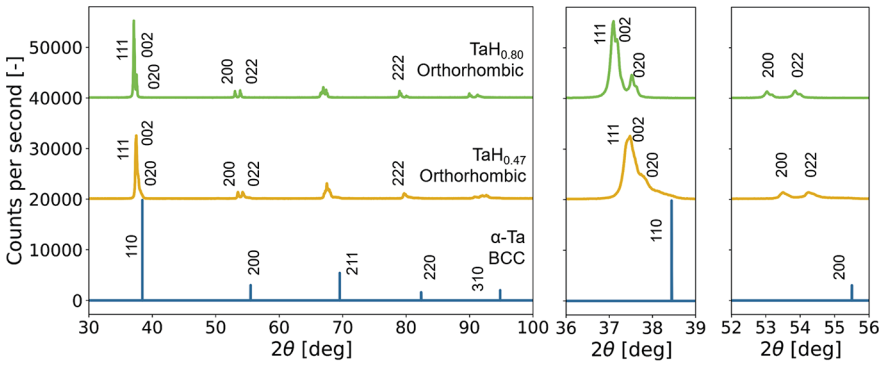

Figure 1. XRD diffraction patterns (Cu Kα, λ = 0.1542 nm) of powder tantalum at two different hydrogenation states: $TaH_{0.47}$ and $TaH_{0.80}$ at 25 °C. The pattern from $TaH_{0.0}$ is included as a reference and is simulated using the unit cell parameters from ref.[38]

top of the sample with respect to the beam, and the range in which the sample height can be adjusted is limited to $-3.0 < z < +3.0$ mm, a 6.0 mm thick aluminum adapter plate was mounted between the sample insert of the reactor chamber and the main body of the chamber. This ensures that the samples were positioned in the center of the goniometer of the diffractometer. The configuration used for the in situ in-plane XRD measurements has on the primary side a Göbel mirror to generate a parallel X-ray beam and a 0.6 mm fixed exit slit. On the secondary side, we used a Sollar 0.2° slit to control the resolution. Both the in-plane and out-of-plane XRD diffraction patterns are fitted with a pseudo-Voight function to obtain the peak position, on the basis of which the d-spacing is calculated using Bragg's law: $n\lambda = 2d_{hkl} \sin\theta$.

Time-of-flight Neutron reflectometry measurements were carried out using the ROG neutron reflectometer. This reflectometer is connected to the 2.3 MW Hoger Onderwijs Reactor (HOR) reactor of the Delft University of Technology, Delft, The Netherlands. The wavelength resolution of $\Delta\lambda/\lambda \approx 2.5\%$ was achieved by setting the double disc chopper to an interdisc distance of 0.280 m and operating the chopper with a frequency of 17.7 Hz and the frame-overlap mirror was set to an angle of 45 mrad. This resulted in a spectrum of $0.11 < \lambda < 1.0$ nm. During the experiments, a fixed incident angle of 8.5 mrad was used, resulting with the given wavelength range in a Q-range of $0.11 < Q < 0.98$ nm^{-1}. To control the angular resolution and footprint on the sample, the vertical gaps of the slits were set to 1.5 and 0.75 mm, for the first and second slits, respectively. Together, this allowed us to achieve a resolution of $\Delta Q/Q \approx 0.05\%$ with a footprint of 80 × 40 mm^2 (umbra/penumbra). A ^{3}He detector was used to detect the neutrons. The samples were hydrogenated at T = 22 °C inside a pressure controlled cell as described elsewhere. To vary the partial hydrogen pressure, the absolute pressure of 0.1% or 4.0% H_2 in Ar gas was stepwise changed between 11 mbar and 6.1 bar ($\Delta c_{H_2}/c_{H_2} < 2\%$, Linde Gas Benelux BV, Dieren, The Netherlands).

The X-ray and neutron reflectometry data were fitted with GenX3,[33,34] yielding estimates for the layer thickness, density, and roughness of each of the three layers of the thin film. As our interest is predominantly in the thickness of the Ta layer and a relatively high correlation exists between the layer thickness of all layers, the thickness of the Ti and $Pd_{0.6}Au_{0.4}$ layer were kept constant in the analysis of the in situ results. As the 10 nm $Pd_{0.6}Au_{0.4}$ layer also expands when exposed to sufficiently high hydrogen pressures, this approach results in a small overestimation of the Ta layer expansion. Subsequently, from the fitted scattering length densities (SLD) and thicknesses of the layers d, we compute the hydrogen concentration x in the Ta layer:

$$x = \left(\frac{\mathrm{SLD}_{\mathrm{TaH}_x}}{\mathrm{SLD}_{\mathrm{Ta}}} \frac{d_{\mathrm{TaH}_x}}{d_{\mathrm{Ta}}} - 1 \right) \frac{b_{\mathrm{Ta}}}{b_{\mathrm{H}}} \quad (1)$$

with $\mathrm{SLD} = \sum_{i=1}^{N} b_i N_i$ the SLD of the layer, b_{Ta} = 6.91 fm and b_{H} = −3.739 fm the scattering lengths of tantalum and hydrogen, respectively,[35] and N_i the number of atoms i per volume unit.[36]

Chunks of Ta with a purity of 99.9 mass % were purchased from Hiranoseizaemonsyouten Co., Ltd. The Ta specimens were set into stainless steel tubes that were evacuated for 1 h at 600 °C. Hydrogen/deuterium absorption at room temperature and desorption under a hydrogen/deuterium pressure of 5 MPa at 600 °C were three times repeated. Hydrogen/deuterium gases of 7N/4N purity were used, respectively. Subsequently, the tube was evacuated for 2 h at 650 °C to dehydrogenate/dedeuterate the samples. Pressure−composition (P−C) isotherms were measured at 25 °C using the volumetric method. Hydride/deuteride specimens with a hydrogen content c_{H} of H/Ta = 0.47 and 0.80 and with a deuterium content c_{D} of D/Ta = 0.48 and 0.84 were obtained by setting a fixed hydrogen/deuterium pressure after measuring the P−C isotherms. The hydrogenated/deuterated samples were deactivated by exposing the powder to air. Each sample kept the respective $c_{\mathrm{H}}/c_{\mathrm{D}}$ for at least a couple of weeks in air.

Powder XRD were performed at room temperature and in air with a Rigaku RINT-2500 V diffratometer (Cu Kα, λ = 0.1542 nm) and with a symmetric θ−2θ scan (Bragg−Brentano). The Rietveld refinement program RIETAN-2000[37] was used to analyze the diffraction patterns. A Rigaku RINT-TTR3 diffractometer (Cu Kα, λ = 0.1542 nm) was used for the temperature-dependent measurements. This diffractometer is equipped with an electric sample heater and gas chamber and features beryllium windows. These temperature-dependent measurements were performed under a helium pressure of 0.15 MPa.

^{2}H magic angle spinning nuclear magnetic resonance (MAS NMR) measurements were carried out using a Bruker Avance 400 spectrometer with a Larmor frequency of 61.423 MHz. Zirconia rotors with an outer diameter of 2.5 mm were filled with the powder samples. A single pulse sequence and a 15 kHz sample spinning rate were used to measure the NMR spectra. A 90° pulse with a length of 3.5 μs was used, and the

https://doi.org/10.1021/acsmaterialslett.3c00038
ACS Materials Lett. 2023, 5, 962−969

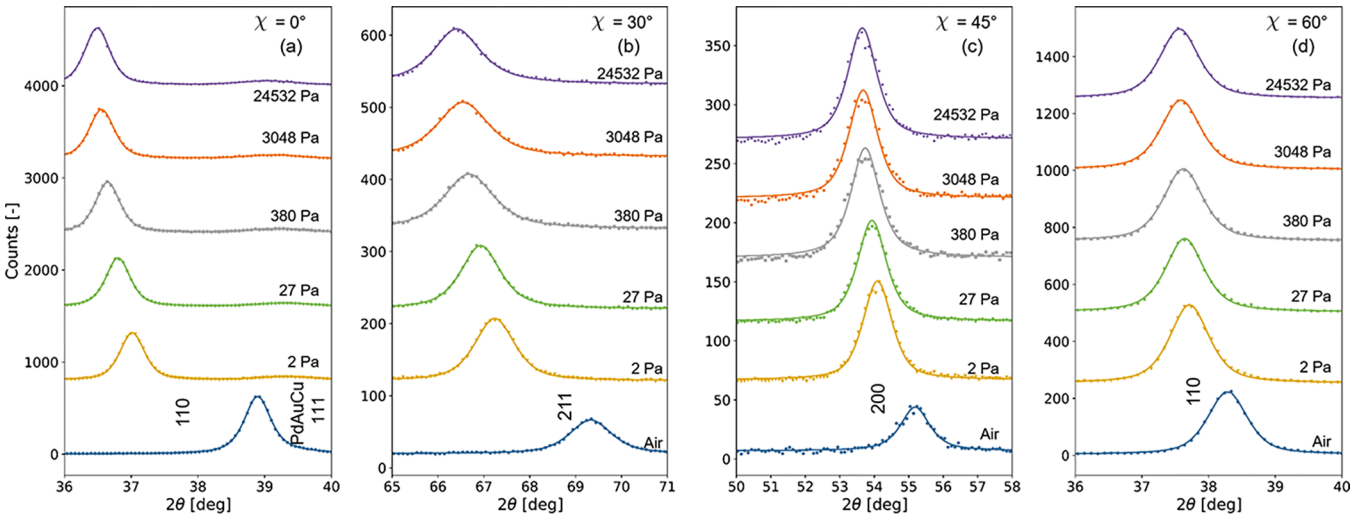

Figure 2. In situ out-of-plane and in-plane XRD measurements (Cu Kα, λ = 0.1542 nm). The measurements were performed on the 40 nm Ta film samples that featured a 3 nm Ti adhesion and a 10 nm $Pd_{0.6}Au_{0.4}$ capping layer at T = 25 °C and for the indicated partial hydrogen pressures P_{H_2}. (a) Out-of-plane diffraction measurements. In-plane diffraction with the sample tilted in the direction perpendicular to the X-ray beam by (b) χ = 30°, (c) χ = 45°, (d) χ = 60°. The continuous lines indicate fits of pseudo-Voigt function(s) to the data used to determine the d-spacing (Figure 3).

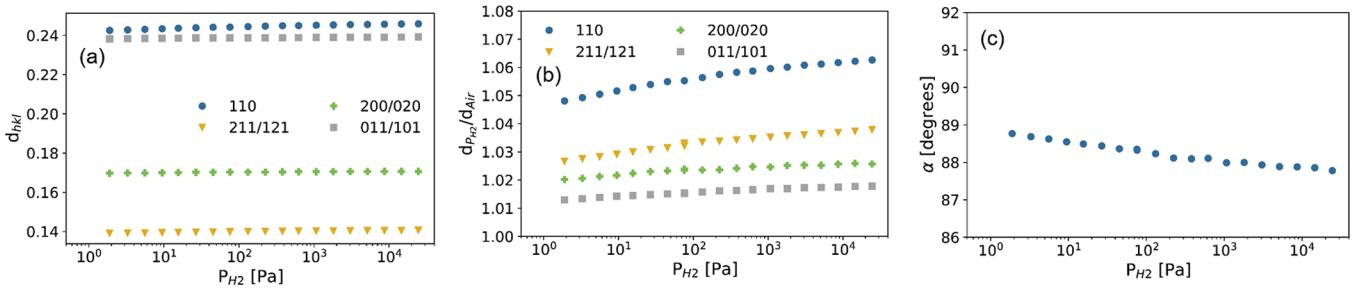

Figure 3. Partial hydrogen dependence of the (a) d-spacing for the (equivalent) reflections indicated, (b) relative expansion of the d-spacing and (c) the angle between the $\vec{a}$ and $\vec{b}$ lattice vectors calculated using eq 2.

recycle delay was set to 1 s. The spectra were referenced to D_2O at 0 ppm.

Before turning to the results on the Ta thin films, we first discuss results on powder Ta to confirm the existence of phase transitions upon hydrogenation at room temperature. Figure 1 displays X-ray diffraction patterns of bcc $TaH_{0.0}$ (simulated using the unit cell parameters reported in ref 38) and of TaH_x at two different hydrogen-to-metal ratios: $TaH_{0.47}$ and $TaH_{0.80}$, obtained from $P-C$ isotherm measurements at 25 °C. Complementary results on deuterated tantalum are reported in Figure S3.

The diffraction patterns of Figure 1 clearly indicate that $TaH_{0.47}$ and $TaH_{0.80}$ have a different phase than $TaH_{0.0}$. Consistent with reports in the literature,[30] careful Rietveld refinement (Figure S2) indicates in both cases a body-centered orthorhombic phase ($C222$) with 4 Ta atoms per unit cell. In the case of $TaH_{0.47}$, the refinement indicates a quasi-tetragonal phase with lattice parameters of a = 0.47327(23) nm, b = 0.34044(16) nm, and c = 0.47680(23) nm and Ta position (0.25, 0.25, 0.7433), resulting in a volume of V = 0.076822 nm^3, i.e., 5.6% expanded with respect to $TaH_{0.0}$ per Ta atom. For $TaH_{0.80}$, refinement resulted in a = 0.48136(15) nm, b = 0.34383(11) nm, c = 0.47740(15) nm, and Ta position (0.25,0.25,0.7460). As such, the unit cell with volume V = 0.079013 nm^3 is thus expanded by about 9.6% per Ta atom. As XRD is not sensitive to the position of the hydrogen atoms in the unit cell, we cannot discriminate between the partially ordered β and fully ordered ϵ orthorhombic phases.

Next, we consider thin film Ta and display in Figure 2 in situ out-of-plane and in-plane diffraction measurements obtained for different partial hydrogen pressures at 25 °C. The thin film was produced by magnetron sputtering and consists of a 4 nm Ti adhesion, a 40 nm Ta, and a 10 nm $Pd_{0.6}Au_{0.4}$ capping layer to promote hydrogen dissociation and prevent oxidation/nitridation of the Ta layer. As the films are highly textured, the out-of-plane results only reveal the 110 reflection. To monitor the other reflections of the bcc unit cell, we performed in-plane in situ diffraction by tilting the sample in the direction perpendicular to the beam by χ = 30, 45, and 60° in order to precisely monitor the hydrogen pressure dependence of the 211, 200, and in-plane 110 reflections.

The XRD patterns measured in air, where the tantalum thin film is completely dehydrogenated, unambiguously reveal that also thin film tantalum crystallizes in a body-centered lattice. When a hydrogen pressure is applied, all reflections shift toward lower diffraction angles, representing an expansion of the lattice while no other peaks emerge (see Figure S9 for the full diffraction patterns).

Results and Conclusions. Most importantly, Figure 3 shows that the shift of the reflection toward lower diffraction angles is

https://doi.org/10.1021/acsmaterialslett.3c00038
ACS Materials Lett. 2023, 5, 962−969

not the same for all reflections, resulting in a deformation of the unit cell. This can most clearly be seen by comparing the out-of-plane and in-plane 110 reflections: whereas at P_{H_2} = 24,600 Pa ($TaH_{0.84}$, as derived from neutron reflectometry (Figure 3(d))), the 110 reflection shifts from 38.8° to 36.6°, the shift of the 011 reflection to 37.5° is much smaller.

Identifying in what way the unit cell is deformed is not easy for thin films. Options include the lattice vectors no longer have the same length, such as for tetragonal ($a = b \neq c$) and orthorhombic ($a \neq b \neq c$) unit cells, or as illustrated in Figure 4, the angle between the lattice vectors is no longer 90°, such

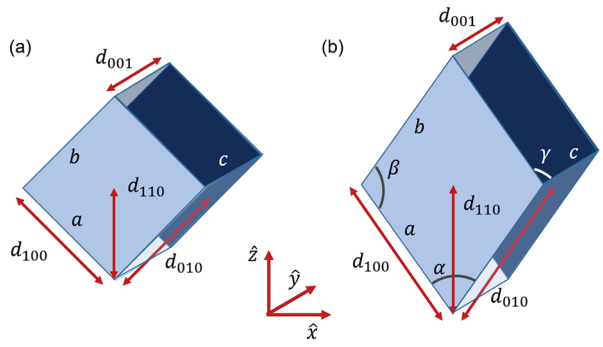

Figure 4. Schematic illustration of (a) an undeformed cubic and (b) deformed unit cell in which the [110] direction is in the out-of-plane direction.

as in a rhomohedral unit cell, or a combination of both (monoclinic/triclinic). As the unit cell in bulk is orthorhombic, we start with exploring this possibility. In an orthorhombic cell, the 200 reflection (which is due to reflections 200, 020, 002, $\bar{2}00$, $0\bar{2}0$, and $00\bar{2}$) splits into three as 200, 020, and 002 are no longer equivalent. With 110 defined out-of-plane, the 200 and 020 reflections are in diffraction condition when the film is rotated by χ = 45°. Looking at the results of Figure 3(c), we only observe one reflection, implying that 200 and 020 are still equivalent and the unit cell is thus not orthorhombic.

To distinguish between a tetragonal and a rhombohedral deformation is more complicated. Ideally, one would consider the 111 reflection which splits for a tetragonal but not for a rhombohedral deformation. However, apart from other problems, this reflection is not allowed for a body-centered unit cell. Another way would be to observe whether the 200 reflection splits into two (tetragonal) or not (rhombohedral). While two of the three reflections can be observed by rotating the film by χ = 45°, the 002 cannot be observed as rotating the film by the required χ = 90° yields hardly any diffracted intensity (and measurements in transmission are not possible due to the substrate). A similar reasoning applies to the 211 reflection.

As such, we consider the ratio between the lattice reflections. Based on the d_{200} and the d_{110} spacings, we can compute the angle between the $\vec{a}$ and $\vec{b}$ lattice vectors α:

$$\alpha = 2 \arccos\left(\frac{d_{110}}{2d_{200}}\right) \tag{2}$$

Substituting the values for d_{110} and d_{200} provides α = 88.0° at P_{H_2} = 24,600 Pa ($TaH_{0.84}$). As shown in Figure 3(c), α shows a gradual and monotonic decrease with increasing P_{H_2}, implying a gradual but steady deformation of the unit cell as the hydrogen concentration in the Ta later increases. While (quasi-)monoclinic unit cells have been reported for bulk Ta, deformations of the unit cell that have been reported do not exceed 0.5° from 90°.[30,39−41]

The only lattice constant for which we did not quantify its expansion is c (Figure 4(b)). To do this, we compute c based on d_{011} obtained by measuring at χ = 60° and d_{200} (χ = 45°):

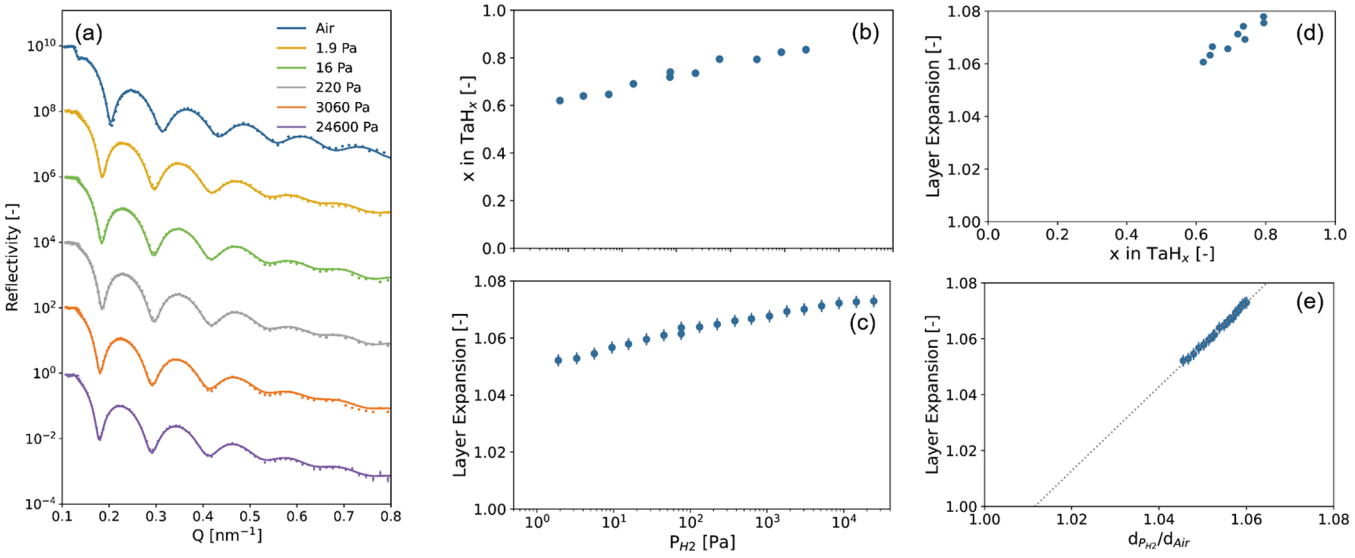

Figure 5. In situ X-ray and neutron reflectometry results to determine the layer expansion and hydrogen concentration of the Ta thin film. (a) Neutron reflectometry data. The continuous lines indicate fits of the data that were used to obtain estimates for the density and layer thickness (see Figure S11 for the corresponding scattering length density profiles and Figure S10 for the corresponding XRR data). Partial hydrogen dependence of the (b) hydrogen concentration of the TaH_x layer and (c) layer expansion as obtained using XRR. (d) Scaling between the layer (volume) expansion of the Ta layer, obtained from XRR (Figure 2(a,c)), and the hydrogen concentration obtained from NR (Figure 2(b,d)). Scaling between (a) the layer (volume) expansion of the Ta layer, obtained from XRR (Figure 2(a,c)), and the out-of-plane d_{110} spacing obtained using XRD (Figure 1(a) and 2(a)). The dotted lines indicate linear fits to the data.

https://doi.org/10.1021/acsmaterialslett.3c00038
ACS Materials Lett. 2023, 5, 962−969

$$c = d_{001} = 2\sqrt{{d_{011}}^2 - {d_{200}}^2} \quad (3)$$

The results, provided in Figure S8, indicate a marginal expansion of the c lattice constant by less than 1%. This is different from a and b, which expand by about 2.5%.

We can increase our confidence in this result by considering the total volumetric expansion of the unit cell. As all the volume expansion in a thin film has to be translated in an increase in layer thickness, we can use XRR to probe the total volumetric expansion. Examining the relationship between the volumetric expansion and d_{110} spacing provides valuable information on how the unit cell deforms. In the case of isotropic cubic expansion, we expect $V = (\sqrt{2}\, d_{110})^3$, whereas a purely tetragonal deformation ($\alpha = \beta = \gamma = 90°$) would result in $V = 2{d_{110}}^2 c$. Differently, in the case where α also alters, we obtain the following relationship:

$$V = 2d_{110}\left(d_{110} \tan\frac{\alpha}{2}\right)c \quad (4)$$

When the volumetric expansion is realized completely out-of-plane, the term $\left(d_{110} \tan\frac{\alpha}{2}\right)$ is constant as the in-plane component of d_{110} expansion is completely offset by a reduction of α. In this scenario, $V = 2d_{110}c$. Since we have shown that c remains practically constant, we expect $V \propto d_{110}$.

The results of Figures S10 and S6 indicate a volumetric expansion of about 7.3% at P_{H_2} = 24,600 Pa ($TaH_{0.84}$), i.e., slightly smaller than the 8% observed for powder Ta. Most importantly, the results of Figure 5(e) indicate that $V \propto d_{110}$ for thin film Ta. We emphasize that, as reported in Figure S12, the partial hydrogen dependence of the d-spacing and volumetric expansion are the same when we measured them by stepwise increasing and decreasing the pressure, implying that there is no hysteresis observed. This is consistent with optical transmission measurements that have been reported before and are reproduced in Figures S13 and S14, indicating the same level of transmission at a given partial hydrogen pressure after an increasing and decreasing pressure step.

The observed proportionality, along with our in-plane in situ diffraction results, reveal that tantalum expands predominantly in the out-of-plane direction by a gradual deformation of the unit cell. As we did not observe any hysteresis, this implies that the deformation is completely elastic. As a result, we would expect that there is a linear relationship between the stress and strain. As the root cause of the expansion of the unit cell is the absorption of hydrogen, we thus expect a linear relationship between the hydrogen concentration in the film and the volumetric expansion.

To determine the hydrogen content in our thin film, we perform in situ neutron reflectometry on our thin films when they are exposed to various partial hydrogen pressures. The results, displayed in Figure 5(b,d) and tabulated in Table S1, indicate a gradual hydrogenation of the thin film with increasing hydrogen pressure, from about $TaH_{0.6}$ at P_{H_2} = 1.9 Pa to about $TaH_{0.84}$ at P_{H_2} = 24,600 Pa alongside a reversible expansion of the layer thickness and increase in the roughness of the layer, which are both reduced again when the partial hydrogen is reduced. The most important observation is that we indeed observe that the volumetric expansion is completely proportional to the hydrogen content. As such, this is consistent with an elastic deformation of the Ta unit cell.

If we compare the response to hydrogen of the thin film to that of powder Ta, we observe two main differences: (i) the suppression of first-order phase transitions and (ii) the elastic deformation of the cubic unit cell. The suppression of phase transitions is a common effect of nanoconfined systems such as thin films clamped to their support. Different from powder materials, two-dimensional clamped films are constrained in their lateral expansion as expansion must be realized only in the out-of-plane direction. This may yield very high in-plane stresses, and the nucleation of domains are considerably hindered as nucleation of domains would locally induce large stresses. As such, it may thermodynamically be unfavorable that such domains are formed at all. In this way, phase transitions may be suppressed in thin films or altered in nature.[17,19−25]

Even when crystalline phase transitions are suppressed, the volumetric expansion to accommodate the hydrogen in the lattice still needs to be realized at least in part. This expansion must take place only in the out-of-plane direction. This implies that lateral expansion of a unit cell is only possible (i) when the film delaminates/buckles from the substrate like in Pd films or (ii) when the host metal atoms' are rearranged in such a way that there a fewer within one layer and the total number of layers increase (see, e.g., ref 42 for illustrations and discussion). Apparently, this scenario is unfavorable in this case, possibly due to the high energy barriers involved in such a rearrangement. Alternatively, the unit cell can also deform and the expansion then takes place purely in the out-of-plane direction, as observed here.

The gradual and elastic deformation of the unit cell over such a wide hydrogen solubility range in a thin film is to the best of our knowledge unique to tantalum. While clamping of a thin film to its support has been shown to have pronounced effects on the occurrence of phase transitions in, e.g., magnesium, vanadium, and palladium thin films[19,25,36,42,43] as well as the potential to deform unit cells,[42] such deformations are usually plastic in nature. We wish to note that (irreversible) changes to the microstructure induced by the hydrogenation, especially upon first exposure to hydrogen, are common to metal hydrides but that we here refer to the size and shape of the unit cell.

The purely elastic deformation upon hydrogenation of Ta and its alloys is of high practical relevance for their use as optical hydrogen sensing materials: it ensures the hysteresis-free response of tantalum to hydrogen within a large hydrogen solubility range. While bulk Ta would be unsuitable for hydrogen sensing owing to the presence of first-order phase transitions and associated hysteresis, thin film Ta is ideal as it thus has a large hydrogen solubility window of about Ta to $TaH_{0.85}$ without any crystalline phase transition. This allows the hysteresis-free sensing of hydrogen over at least 7 orders of magnitude in pressure and an optical response that is stable over time and repeated exposure to hydrogen.[26−28,44]

In conclusion, we have shown that the hydrogenation of Ta(110) thin films induces a substantial deformation of the bcc Ta unit cell. Different from powder Ta, we do not observe any (first-order) phase transition, showing a pronounced effect of the clamping of the Ta film to the support. Differently, to accommodate hydrogen, the tantalum unit cell expands predominantly in the out-of-plane direction. In doing so, the unit cell deforms gradually with increasing hydrogen concentration, with the results that the a and b lattice constants are no longer equal to the c lattice constant and that

https://doi.org/10.1021/acsmaterialslett.3c00038
ACS Materials Lett. 2023, 5, 962−969

the angle between the $\vec{a}$ and $\vec{b}$ lattice vectors deviates from 90°. Surprisingly, this deformation is completely elastic in nature. This positions Ta (and its alloys) as an attractive hydrogen sensing material as the large solubility window within one phase and the absence of plastic deformation ensures the hysteresis-free sensing of hydrogen over at least 7 orders of magnitude in pressure. In a more general perspective, the results show that nanoconfinement can tailor the properties of metal hydrides and boost their performance as functional materials.

■ ASSOCIATED CONTENT

Supporting Information

The Supporting Information is available free of charge at https://pubs.acs.org/doi/10.1021/acsmaterialslett.3c00038.

AFM measurement of the thin film sample, XRD patterns and corresponding Rietveld refinements of powder $TaH_{0.47}$ and $TaH_{0.80}$, XRD patterns and corresponding Rietveld refinements of powder $TaD_{0.48}$ and $TaD_{0.84}$, temperature-dependent XRD on $TaD_{0.48}$ and $TaD_{0.84}$, NMR measurements of powder $TaD_{0.48}$ and $TaD_{0.84}$, temperature-dependent NMR on $TaD_{0.48}$ and $TaD_{0.84}$, full XRD patterns of Ta films, XRR results, scattering length density (SLD) profiles of the in situ XRR and NR results, fitted neutron reflectometry parameters, measurements of the Ta *d*-spacing and layer thickness after increasing and decreasing pressure steps, optical transmission measurements (PDF)

■ AUTHOR INFORMATION

Corresponding Author

Lars J. Bannenberg − *Faculty of Applied Sciences, Delft University of Technology, 2629 JB Delft, The Netherlands;* orcid.org/0000-0001-8150-3694; Email: l.j.bannenberg@tudelft.nl

Authors

Larissa Blom − *Faculty of Applied Sciences, Delft University of Technology, 2629 JB Delft, The Netherlands*

Kouji Sakaki − *Energy Process Research Institute, National Institute of Advanced Industrial Science and Technology (AIST), Tsukuba, Ibaraki 305-8569, Japan;* orcid.org/0000-0003-4781-1073

Kohta Asano − *Energy Process Research Institute, National Institute of Advanced Industrial Science and Technology (AIST), Tsukuba, Ibaraki 305-8569, Japan;* orcid.org/0000-0003-4208-7303

Herman Schreuders − *Faculty of Applied Sciences, Delft University of Technology, 2629 JB Delft, The Netherlands*

Complete contact information is available at: https://pubs.acs.org/10.1021/acsmaterialslett.3c00038

Notes

The authors declare no competing financial interest.

■ ACKNOWLEDGMENTS

Support by Kees de Vroege, Piet van der Ende and Raymon Bresser with the neutron reflectometry measurements is greatly appreciated. Bart Boshuizen is acknowledged for designing and maintaining the Labview software to control the pressure cells. We thank Erwin Janssen for providing and connecting the gas cylinders and reducers and Marcel Bus for the AFM measurement.

■ REFERENCES

(1) Rusman, N. A. A.; Dahari, M. A Review on the Current Progress of Metal Hydrides Material for Solid-State Hydrogen Storage Applications. *Int. J. Hydrogen Energy* **2016**, *41*, 12108−12126.

(2) Schneemann, A.; White, J. L.; Kang, S.; Jeong, S.; Wan, L. F.; Cho, E. S.; Heo, T. W.; Prendergast, D.; Urban, J. J.; Wood, B. C.; Allendorf, M. D.; Stavila, V. Nanostructured Metal Hydrides for Hydrogen Storage. *Chem. Rev.* **2018**, *118*, 10775−10839.

(3) Bannenberg, L. J.; et al. Metal (boro-) Hydrides for High Energy Density Storage and Relevant Emerging Technologies. *Int. J. Hydrogen Energy* **2020**, *45*, 33687−33730.

(4) Lototskyy, M. V.; Tolj, I.; Pickering, L.; Sita, C.; Barbir, F.; Yartys, V. The Use of Metal Hydrides in Fuel Cell Applications. *Progress in Natural Science: Materials International* **2017**, *27*, 3−20.

(5) Nishimura, C.; Komaki, M.; Hwang, S.; Amano, M. V−Ni alloy Membranes for Hydrogen Purification. *J. Alloys Compd.* **2002**, *330*, 902−906.

(6) Dolan, M. D.; Viano, D. M.; Langley, M. J.; Lamb, K. E. Tubular Vanadium Membranes for Hydrogen Purification. *J. Membr. Sci.* **2018**, *549*, 306−311.

(7) Zeng, L.; Kawahito, K.; Ikeda, S.; Ichikawa, T.; Miyaoka, H.; Kojima, Y. Metal hydride-based materials towards high performance negative electrodes for all-solid-state lithium-ion batteries. *Chem. Commun.* **2015**, *51*, 9773−9776.

(8) Ovshinsky, S. R.; Fetcenko, M. A.; Ross, J. A nickel metal hydride battery for electric vehicles. *Science* **1993**, *260*, 176−181.

(9) Huiberts, J. N.; Griessen, R.; Rector, J. H.; Wijngaarden, R. J.; Dekker, J. P.; De Groot, D. G.; Koeman, N. J. Yttrium and Lanthanum Hydride Films with Switchable Optical Properties. *Nature* **1996**, *380*, 231−234.

(10) Maiorov, V. A. Metal Hydride Switchable Mirrors. *Opt. Spectrosc.* **2020**, *128*, 148−165.

(11) Hübert, T.; Boon-Brett, L.; Black, G.; Banach, U. Hydrogen Sensors−a Review. *Sens. Actuators, B* **2011**, *157*, 329−352.

(12) Wadell, C.; Syrenova, S.; Langhammer, C. Plasmonic Hydrogen Sensing with Nanostructured Metal Hydrides. *ACS Nano* **2014**, *8*, 11925−11940.

(13) Bannenberg, L. J.; Boelsma, C.; Asano, K.; Schreuders, H.; Dam, B. Metal Hydride Based Optical Hydrogen Sensors. *J. Phys. Soc. Jpn.* **2020**, *89*, 051003.

(14) Darmadi, I.; Nugroho, F. A. A.; Langhammer, C. High-Performance Nanostructured Palladium-Based Hydrogen Sensors−Current Limitations and Strategies for Their Mitigation. *ACS Sensors* **2020**, *5*, 3306−3327.

(15) Koo, W.-T.; Cho, H.-J.; Kim, D.-H.; Kim, Y. H.; Shin, H.; Penner, R. M.; Kim, I.-D. Chemiresistive Hydrogen Sensors: Fundamentals, Recent Advances, and Challenges. *ACS Nano* **2020**, *14*, 14284−14322.

(16) Chen, K.; Yuan, D.; Zhao, Y. Review of Optical Hydrogen Sensors Based on Metal Hydrides: Recent Developments and Challenges. *Optics & Laser Technology* **2021**, *137*, 106808.

(17) Feenstra, R.; de Bruin-Hordijk, G. J.; Bakker, H. L. M.; Griessen, R.; de Groot, D. G. Critical Point Lowering in Thin PdH_x Films. *Journal of Physics F: Metal Physics* **1983**, *13*, L13.

(18) Pivak, Y.; Gremaud, R.; Gross, K.; Gonzalez-Silveira, M.; Walton, A.; Book, D.; Schreuders, H.; Dam, B.; Griessen, R. Effect of the Substrate on the Thermodynamic Properties of PdH_x Films Studied by Hydrogenography. *Scripta Materialia* **2009**, *60*, 348−351.

(19) Bloch, J.; Pejova, B.; Jacob, J.; Hjörvarsson, B. Hydrogen-vanadium system in thin films: Effect of film thickness. *Phys. Rev. B* **2010**, *82*, 245428.

(20) Baldi, A.; Narayan, T. C.; Koh, A. L.; Dionne, J. A. In situ detection of hydrogen-induced phase transitions in individual palladium nanocrystals. *Nat. Mater.* **2014**, *13*, 1143−1148.

(21) Syrenova, S.; Wadell, C.; Nugroho, F. A.; Gschneidtner, T. A.; Fernandez, Y. A. D.; Nalin, G.; Świtlik, D.; Westerlund, F.;

Antosiewicz, T. J.; Zhdanov, V. P.; et al. Hydride Formation Thermodynamics and Hysteresis in Individual Pd Nanocrystals with Different Size and Shape. *Nat. Mater.* **2015**, *14*, 1236−1244.
(22) Griessen, R.; Strohfeldt, N.; Giessen, H. Thermodynamics of the Hybrid Interaction of Hydrogen with Palladium Nanoparticles. *Nat. Mater.* **2016**, *15*, 311−317.
(23) Burlaka, V.; Wagner, S.; Hamm, M.; Pundt, A. Suppression of Phase Transformation in Nb−H Thin Films below Switchover Thickness. *Nano Lett.* **2016**, *16*, 6207−6212.
(24) Wagner, S.; Pundt, A. Quasi-Thermodynamic Model on Hydride Formation in Palladium−Hydrogen Thin Films: Impact of Elastic and Microstructural Constraints. *Int. J. Hydrogen Energy* **2016**, *41*, 2727−2738.
(25) Bannenberg, L. J.; Nugroho, F. A. A.; Schreuders, H.; Norder, B.; Trinh, T. T.; Steinke, N.-J.; Van Well, A. A.; Langhammer, C.; Dam, B. Direct Comparison of PdAu Alloy Thin Films and Nanoparticles upon Hydrogen Exposure. *ACS Appl. Mater. Interfaces* **2019**, *11*, 15489−15497.
(26) Bannenberg, L. J.; Boelsma, C.; Schreuders, H.; Francke, S.; Steinke, N.-J.; Van Well, A. A.; Dam, B. Optical Hydrogen Sensing Beyond Palladium: Hafnium and Tantalum as Effective Sensing Materials. *Sens. Actuators, B* **2019**, *283*, 538−548.
(27) Bannenberg, L. J.; Schreuders, H.; Dam, B. Tantalum-Palladium: Hysteresis-Free Optical Hydrogen Sensor over 7 Orders of Magnitude in Pressure with Sub-Second Response. *Adv. Funct. Mater.* **2021**, *31*, 2010483.
(28) Bannenberg, L. J.; Schreuders, H.; van Beugen, N.; Kinane, C.; Hall, S.; Dam, B. Tuning the properties of thin film TaRu for hydrogen sensing applications. *ACS Appl. Mater. Interfaces* **2023**, *15*, 8033.
(29) Pryde, J. A.; Tsong, I. S. T. A theory of the resistivity of high-concentration interstitial alloys with application to the tantalum-hydrogen and tantalum-deuterium systems. *Acta Metall.* **1971**, *19*, 1333−1338.
(30) San-Martin, A.; Manchester, F. D. The H-Ta (Hydrogen-Tantalum) System. *J. Phase Equilib.* **1991**, *12*, 332−343.
(31) Saba, W. G.; Wallace, W. E.; Sandmo, H.; Craig, R. S. Heat capacities and the residual entropy of Ta2H. *J. Chem. Phys.* **1961**, *35*, 2148−2155.
(32) Berlincourt, T. G.; Bickel, P. W. Electrical Properties of Ta2H. *Phys. Rev. B* **1970**, *2*, 4838.
(33) Björck, M.; Andersson, G. GenX: an Extensible X-ray Reflectivity Refinement Program Utilizing Differential Evolution. *J. Appl. Crystallogr.* **2007**, *40*, 1174−1178.
(34) Glavic, A.; Björck, M. GenX 3: the latest generation of an established tool. *J. Appl. Crystallogr.* **2022**, *55*, 1063−1071.
(35) Sears, V. F. Neutron scattering lengths and cross sections. *Neutron news* **1992**, *3*, 26−37.
(36) Bannenberg, L. J.; Schreuders, H.; van Eijck, L.; Heringa, J. R.; Steinke, N.-J.; Dalgliesh, R.; Dam, B.; Mulder, F. M.; van Well, A. A. Impact of Nanostructuring on the Phase Behavior of Insertion Materials: The Hydrogenation Kinetics of a Magnesium Thin Film. *J. Phys. Chem. C* **2016**, *120*, 10185−10191.
(37) Izumi, F.; Ikeda, T. A rietveld-analysis programm RIETAN-98 and its applications to zeolites. *Mater. Sci. Forum* **2000**, *321-324*, 198−205.
(38) Vavilova, V. V.; Galkin, L. N.; Glazov, M. V. Stabilization of a Phase With the delta-Mn Structure by Rapid Quenching in the Rhenium−Tantalum System. *Dokl. Akad. Nauk SSSR.* **1988**, 1157−1161.
(39) X-ray analysis and magnetic susceptibilities of tantalum hydrides, author = Stalinski, B. *Bull. Acad. Polon. Sci. Cl* **1954**, *3*, 245.
(40) Ducastelle, F.; Caudron, R.; Costa, P. Study of the Ta-H System: Equilibrium Diagram and Electronic Structure. *J. PHYSICS CHEM SOLIDS* **1970**, *31*, 1247−1256.
(41) Yamada, R.; Watanabe, N.; Sato, K.; Asano, H.; Hirabayashi, M. Localized modes in tantalum hydrides studied by neutron inelastic scattering. *J. Phys. Soc. Jpn.* **1976**, *41*, 85−90.
(42) Pivak, Y.; Schreuders, H.; Slaman, M.; Griessen, R.; Dam, B. Thermodynamics, Stress Release and Hysteresis Behavior in Highly Adhesive Pd−H Films. *Int. J. Hydrogen Energy* **2011**, *36*, 4056−4067.
(43) Bannenberg, L. J.; Schreuders, H.; Kim, H.; Sakaki, K.; Hayashi, S.; Ikeda, K.; Otomo, T.; Asano, K.; Dam, B. Suppression of the Phase Coexistence of the fcc−fct Transition in Hafnium-Hydride Thin Films. *J. Phys. Chem. Lett.* **2021**, *12*, 10969−10974.
(44) Bannenberg, L. J.; Boshuizen, B.; Ardy Nugroho, F. A.; Schreuders, H. Hydrogenation kinetics of metal hydride catalytic layers. *ACS Appl. Mater. Interfaces* **2021**, *13*, 52530−52541.

https://doi.org/10.1021/acsmaterialslett.3c00038
ACS Materials Lett. 2023, 5, 962−969